$O(^1S)$, OH, and $O_2(b)$ airglow layer perturbations due to AGWs and their implied effects on the atmosphere

Fabio Vargas,[1,2] Gary Swenson,[1] Alan Liu,[1] and Delano Gobbi[3]

Received 12 June 2006; revised 8 December 2006; accepted 17 December 2006; published 19 July 2007.

[1] The $O(^1S)$ (green line) night airglow emission in response to atmospheric gravity wave (AGW) perturbations was simulated with a linear, one-dimensional model. The results were combined with previously modeled O_2(b, 0–1) atmospheric band and OH Meinel band emission response (Liu and Swenson, 2003) to derive amplitude and phase relations among multiple airglow layers in response to gravity waves with various intrinsic parameters and damping rates (β). The simulations show that the vertical profile of the standard deviation of the perturbed green line volume emission rate (VER) has a centroid altitude that is 3 km lower and a full-width-half-maximum 2.1 km smaller than the unperturbed VER profile, similar to findings for the OH and O_2(b) band layers. Relative phase differences and amplitudes of vertically propagating waves can be deduced from zenith observations of the layers. Airglow weighted responses to waves are related through a cancellation factor (CF) for both layer intensity and temperature. The vertical wavelength can be deduced from relative phase information of three airglow layers separated in altitude. The vertical flux of horizontal momentum associated with gravity waves is deduced from intrinsic wave parameters. Wave damping versus altitude is used to deduce the flux divergence and local accelerations resulting from dissipative waves. The simulations are useful in calculating wave information and wave effects on the atmosphere from multiwavelength, zenith airglow observations.

Citation: Vargas, F., G. Swenson, A. Liu, and D. Gobbi (2007), $O(^1S)$, OH, and O_2(b) airglow layer perturbations due to AGWs and their implied effects on the atmosphere, *J. Geophys. Res.*, *112*, D14102, doi:10.1029/2006JD007642.

1. Introduction

[2] Atmospheric gravity waves (AGWs) play important roles in the dynamics of the upper atmosphere and lower thermosphere. Because they are able to transport energy and momentum from lower atmosphere into the mesospheric region, there is great interest in quantifying these fluxes and determining how these waves affect that region [e.g., *Fritts and Dunkerton*, 1985]. Measurements of AGWs with radar performed by *Fritts and Vincent* [1987] showed that 70% of the momentum flux in the mesosphere region is transported by gravity waves with periods less than one hour, causing an acceleration of 20–100 m s^{-1} day^{-1} on the mean flow.

[3] Relatively recent efforts to determine the momentum fluxes of AGWs use low-cost, high-performance CCD optical devices that provide images of the airglow layers. Those layers are natural tracers of AGWs in the mesopause region. As addressed in several papers, it is possible to determine the intrinsic parameters of AGWs from image data [e.g., *Hecht et al.*, 1994; *Taylor et al.*, 1995; *Coble et al.*, 1998; *Nakamura et al.*, 1999, 2001; *Hecht et al.*, 2001; *Gavrilyeva and Ammosov*, 2002; *Suzuki et al.*, 2004] and to use these data to calculate the energy and momentum fluxes [e.g., *Swenson and Liu*, 1998; *Swenson et al.*, 1999; *Espy et al.*, 2004; *Tang et al.*, 2005]. An important concept is the cancellation factor (CF) introduced by *Swenson and Gardner* [1998] for OH airglow, is a quantitative factor relating the observed zenith-viewed intensity perturbation to the wave amplitudes. This differs from the Krassovsky ratio, which is discussed later in this paper and was thoroughly discussed by *Swenson and Gardner* [1998] where CF was originally introduced for OH.

[4] For waves observed simultaneously in two or more airglow layers separated in altitudes in the mesopause region, it is possible to characterize the flux convergence, hence their effect on the background atmosphere. In this study, we simulate the dynamic response of the $O(^1S)$ layer to gravity waves using the model similar to that described by *Liu and Swenson* [2003] for OH and O_2(b) emission layers. We have closely followed their approach, but our main goal here is to relate the momentum and energy fluxes versus vertical wavelength and damping rates, and flux convergence between the different airglow layers. Modeled variables including CFs, amplitudes, layer intensities (I'), rotational temperature (T'_m), and phase differences for all three layers (OH, O_2(b) and $O(^1S)$) are calculated and compared. These relations are used to derive AGW param-

[1]Department of Electrical and Computer Engineering, University of Illinois at Urbana-Champaign, Urbana, Illinois, USA.
[2]Also at Aeronomy Division, National Institute for Space Research, São José dos Campos, Brazil.
[3]Aeronomy Division, National Institute for Space Research, São José dos Campos, Brazil.

0148-0227/07/2006JD007642

eters from multilayer airglow observations as well as to deduce momentum and energy fluxes from those observations.

[5] The paper is structured as follows. Section 2 describes the photochemistry of $O(^1S)$, $O_2(b)$ and OH, and volume emission rate, intensity and weighted temperature calculations. The previous modeling of $O_2(b)$ and OH from *Liu and Swenson* [2003] is summarized for convenience. Dynamic equations used to model the wave disturbance and the responses of the atmosphere are described in section 3. The results of the simulations are shown in section 4. In section 5 we calculate the flux of momentum and energy and their convergence assuming damped AGWs. A summary is presented in section 6.

2. $O(^1S)$ Photochemistry

[6] The most probable process leading to $O(^1S)$ production is the Barth mechanism [*Barth*, 1961]. It occurs in two steps, involving first the recombination of the oxygen followed by the energetic deactivation of the excited precursor O_2^*. These processes are summarized as:

$$\begin{aligned} O + O + M(O_2 + N_2) &\longrightarrow O_2^* + M \\ O_2^* + O &\longrightarrow O(^1S) + O_2 \end{aligned} \tag{1}$$

Quenching losses must also be considered for both $O(^1S)$ and O_2^*. This set of photochemical reactions leads to the following volume emission rate [*McDade et al.*, 1986, *Murtagh et al.*, 1990]:

$$\varepsilon_{O(^1S)} = A_5\left[O(^1S)\right] = \frac{A_5 k_1 [O]^3([O_2] + [N_2])}{(A_6 + k_5[O_2])(15[O_2] + 211[O])} \tag{2}$$

where $k_1 = 4.7 \times 10^{-33}$ $(300/T)^2$ cm^6 s^{-1} is the rate coefficient of three-body recombination of atomic oxygen, $k_5 = 4.0 \times 10^{-12}$ exp(−865/T)cm^3 s^{-1} is the rate coefficient for quenching of $O(^1S)$ by atmospheric O_2, $A_5 = 1.18$ s^{-1} is the probability of transition between the state ^1S to the state ^1D, and $A_6 = 1.35$ s^{-1} is the $O(^1S)$ total transition probability. [*] represents number density.

[7] For reference we include here the photochemistry of the $O_2(b)$ and OH(8−3) adopted by *Liu and Swenson* [2003] and used in this paper. The VER of $O_2(b)$ is calculated using the two-step mechanism as described above. The excited state $O_2(c^1\Sigma_u^-)$ is created through the three-body recombination reaction, followed by the reaction with ground state molecular oxygen, generating the $O_2(b^1\Sigma_g^-)$ atmospheric band [*McDade et al.*, 1986; *Murtagh et al.*, 1990]. The volume emission rate for this emission is given by:

$$\varepsilon_{O_2} = \frac{A_1 k_1 [O]^2 [O_2]([O_2] + [N_2])}{\left(A_2 + k_2^{O_2}[O_2] + k_2^{N_2}[N_2]\right)(7.5[O_2] + 33[O])} \tag{3}$$

where k_1 is again the three-body recombination coefficient, $A_1 = 0.079$ s^{-1} is the (0−0) band transition probability, $A_2 = 0.083$ s^{-1} is the inverse radiative lifetime of the excited $O_2(b^1\Sigma_g^+ \cdot \nu = 0)$, and the quenching coefficients $k_2^{O_2} = 4 \times 10^{-17}$ cm^3 s^{-1} and $k_2^{N_2} = 2.2 \times 10^{-15}$ cm^3 s^{-1}. The values of these reaction coefficients used in our calculations for $\varepsilon_{O(^1S)}$ and ε_{O_2} are from *McDade et al.* [1986] and were widely used in other studies [e.g., *Murtagh et al.*, 1990].

[8] The OH Meinel band spectrum is generated by the reaction of ozone with hydrogen. The explicit expression for the VER profile in terms of O, O_2 and N_2 number densities is given by *McDade et al.* [1987]:

$$\varepsilon_{OH} = \frac{f_8[O][O_2]\left(k_6^{O_2}[O_2] + k_6^{N_2}[N_2]\right)}{260 + 2 \times 10^{11}[O_2]} \tag{4}$$

where the quenching coefficients are $k_6^{O_2} = 5.96 \times 10^{-34}(300/T)^{2.37}$ cm^3 s^{-1} and $k_6^{N_2} = 5.7 \times 10^{-34}(300/T)^{2.62}$ cm^3 s^{-1}, and $f_8 = 0.29$ is the fraction of the $H + O_3$ production into the vibrational level $\nu = 8$. The photochemistry adopted in here is for the OH(8−3) vibrational transition and follows *McDade et al.* [1987, and references therein].

[9] The intensity of a zenith-viewed airglow emission is the vertical integral of the VER over the entire layer (VERs are given in unit of photons cm^{-3} s^{-1}):

$$I(t) = \int_{z_0}^{z_1} \varepsilon(z,t)dz \tag{5}$$

where z_0 and z_1 are taken to be 75 and 110 km, respectively, which includes all 3 airglow layers. We also define the intensity weighted temperature T_m in the layer by:

$$T_m(t) = \frac{\int_{z_0}^{z_1} \varepsilon(z,t)T(z,t)dz}{\int_{z_0}^{z_1} \varepsilon(z,t)dz} \tag{6}$$

For OH and $O_2(b)$ layers, T_m represents the rotational temperature of OH and $O_2(b)$ molecules. For the atomic oxygen, there is no rotational temperature, but we can still define this equivalent layer weighted temperature for comparison with other layers. *Makhlouf et al.* [1995] performed a study suggesting the brightness weighted OH rotational temperature could differ by 10−20 K of that of the Doppler temperature. A recent study by *Zhao et al.* [2005] demonstrates that the volume weighted lidar measured temperature profiles compare extremely well to OH and $O_2(b)$ rotational temperatures when altitudes of the layers are considered as the layers are elevated (or lowered) by the tidal waves. The RMS temperature differences between rotational and lidar Doppler measurements were found to be less than 4 K under most circumstances, which is near the combined measurement uncertainty.

3. Model Description

[10] We used a one-dimensional linear model to describe the temporal and spatial variability of the airglow volume emission rate, intensity and weighted temperature due to upward propagating internal gravity waves. We assumed a vertical structure of a monochromatic wave for perturbations in temperature T' and density ρ' as:

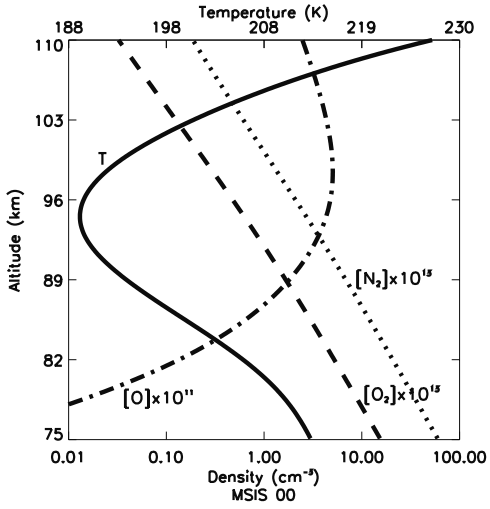

Figure 1. Background atmosphere taken from the MSIS00 model. The vertical profiles show the temperature (solid line), atomic oxygen (dash-dotted line), molecular oxygen (dashed line), and molecular nitrogen (dotted line) densities calculated for 35°N on 21 March 1994 (0000 LT) for low solar and geomagnetic activity.

$$(T'/T_u, \rho'/\rho_u) = \Re\left\{ (\hat{T}, \hat{\rho}) e^{\alpha z^* + i\left(mz^* + \omega t\right)} \right\}, \tag{7}$$

where m is the vertical wavelength, $\alpha = (1 - \beta)/2H$, ω is the intrinsic frequency, H the atmospheric density scale height, and $z^* = z - z_r$, where $z_r = 85$ km is a reference altitude; T_u and ρ_u are unperturbed temperature and density, and $\hat{T}$ and $\hat{\rho}$ are complex amplitudes, respectively. The exponential term in (7) does not include horizontal wave number since our simulation is one-dimensional.

[11] The parameter β represents the damping rate and characterizes the amplitude growth of the wave. $\beta = 0$ represents a freely propagating wave with amplitude growing exponentially with altitude, e-folding every two scale heights. $\beta = 1$ represents a saturated wave with no amplitude change with altitude. $\beta > 1$ represents a strongly damped wave with its amplitude decreasing with increasing altitude. For a sample of high-frequency (period < 30 min) wave measurements made in Albuquerque, NM and Maui, HI, the damping characteristics of waves observed by lidar were shown to be saturated or supersaturated [*Swenson et al.*, 2003]. Comparisons of modeled layer brightness with layer measurements in this study will hopefully contribute to more multiwavelength observations of wave amplitudes (and damping) so that, in the future, statistics on damping can be deduced.

[12] The intrinsic frequency ω and vertical wave number m are related to the horizontal wave number k through the dispersion relation [*Hines*, 1960]:

$$m^2 = \frac{N^2 - \omega^2}{\omega^2 - f^2} k^2 - \frac{1}{4H^2} + \frac{\omega^2}{\gamma g H}, \tag{8}$$

where N is the Brünt-Väisälä frequency, f the inertial frequency, $\gamma = c_p/c_v$ the ratio of specific heats and g the acceleration of gravity ~ 9.5 ms^{-2}. In this model the gravity waves are modeled with the linear theory and the background atmosphere is windless. Nonlinear effects are not included. These results apply to small amplitude waves.

[13] The complex amplitudes in the equation (7) are related through the polarization relations as [*Walterscheid et al.*, 1987; *Zhang et al.*, 1993]:

$$\hat{\rho} = \frac{1 - 2\omega^2 H/[g(\gamma - 1)] - 2iHm}{1 - 2\omega^2 H/g + 2iHm} \hat{T}. \tag{9}$$

[14] The background atmosphere used here was obtained from the MSIS00 model [*Picone et al.*, 2002]. Figure 1 shows the profiles of temperature and the number densities of N_2, O_2 and O computed for spring equinox at 35°N, at low solar and geomagnetic activity ($F_{10.3} = 130$ and Ap = 15). Because N_2 and O_2 are well mixed below the mesopause, their perturbations can be associated with the atmospheric density perturbation as

$$\frac{[O_2]'}{[O_2]_u} = \frac{[N_2]'}{[N_2]_u} = \frac{\rho'}{\rho_u}. \tag{10}$$

[15] Because [O] is dependent on both temperature and density, and because it is not uniformly distributed in the low thermosphere, its perturbation is calculated as [*Zhang et al.*, 1993]:

$$\frac{[O]'}{[O]_u} = DH \frac{\rho'}{\rho_u} + \frac{1 - DH}{\gamma - 1} \frac{T'}{T_u}, \tag{11}$$

where $D = -d(\ln[O])/dz$ is the inverse of the scale height of the [O]. At the altitude where $DH = 1$, i.e., the scale height of oxygen equals the scale height of the dominant gas, the relative perturbation of [O] becomes the same as in (10). As shown in equation (2) for the green line, the change of volume emission rate is primarily due to change of [O], which is associated with vertical movement of O rich/poor air by wave perturbations, although it is also slightly affected by temperature variation through the reaction coefficients.

[16] In order to derive gravity wave amplitudes from airglow measurement, it is necessary to obtain the relation between airglow intensity perturbation and gravity waves. Because of the finite thickness of the airglow layer, cancellation occurs within layer for waves with vertical wavelengths which are on the order of, or less than the layer thickness. The CF introduced by *Swenson and Gardner* [1998] is the parameter that quantifies this cancellation effect. CF_I (CF_{Tm}) is defined as the ratio of the airglow intensity (temperature) perturbation amplitude to the gravity wave amplitude. CF should not be confused with the Krassovsky parameter η [*Krassovsky*, 1972], which is defined as the ratio of relative intensity ($I'/\overline{I}$) to the relative volume emission rate weighted temperature ($T'_m/\overline{T}_m$). Because η is a ratio between two quantities both of which are weighted by the VER profile, it does not represent the cancellation effect, which primarily results from the integral effects of a vertical wavelength propagating through a layer with a finite thickness. Once the CF is known, gravity wave

amplitudes can be deduced from the measured airglow intensity perturbation amplitude.

[17] The model simulation is done as following. A wave perturbation of 1% amplitude in temperature at a reference altitude, z_r = 85 km, is specified according to (7). The atmospheric density perturbation is then calculated with the polarization relation (9). Perturbations in $[O_2]$, $[N_2]$ and [O] are calculated using equations (10) and (11). Perturbed VER profiles are obtained from expressions (2), (3) and (4), where the reaction coefficients depend on the perturbed temperature. This is repeated for wave perturbations varying over an entire period. For each calculated VER profile, the intensity, I, and the layer weighted temperature, T_m, are also calculated. The time series of I and T_m are fitted to a sinusoidal function to determine their amplitude and phase.

[18] The major assumptions made for this one-dimensional model of the atmospheric waves (including AGWs and tides) producing atmospheric emission layer perturbations in normal viewing intensity and layer weighted temperatures are summarized. This includes the following:

[19] 1. The wave amplitudes are small so that we can use the linear equations to describe AGWs using their polarization and dispersion relationships.

[20] 2. The background atmosphere specified by the MSIS00 model is unchanged by the waves. It determines the composition and temperature through which the waves are propagating.

[21] 3. The atmosphere is windless (and of course no shear with altitude). In practice, intrinsic wave periods need to be deduced to apply the results of the model. The background wind used to deduced the intrinsic period should be weighted by standard derivation profiles discussed later in section 4.

[22] 4. The waves are propagating vertically (and are not ducted, for example). The waves are assumed to extend through the layers modeled.

4. Results and Discussion

[23] The simulations were done for varying vertical wavelength λ and damping coefficient β. To help understand the results, we present the simulations in three steps. First, we present the results for a single AGW with a fixed set of λ and β, in order to investigate in detail the relationship between wave perturbations and VERs. Second, we present the simulations with varying λ but with a constant β to focus on the effects of λ only. Last, we present the results with both varying λ and β with a focus on the effect of wave damping. The OH and O_2(b) simulations from previous work by *Liu and Swenson* [2003] were also repeated with identical wave parameter settings used in the $O(^1S)$ simulation. The results for the three layers are calculated and compared and their amplitude ratios and phase differences are discussed.

4.1. Constant λ_z and β

[24] We first focus on the response of VER to a gravity wave with a period of two hours, λ = 25 km, and damping coefficient β = 1 (a saturated wave). The horizontal wavelength calculated from dispersion relation for this wave is 580 km. The simulated VERs for all three airglow layers are shown in Figure 2. Figures 2a–2c show profiles of the unperturbed and perturbed VER profiles. The VER profiles are shown with 15° phase steps for the 2 hour wave period. The centroid altitude of undisturbed profiles (thick straight line) are located on 89.9 km, 95 km and at 97.3 km for OH, O_2(b) and $O(^1S)$ layers, respectively. Also plotted in Figures 2a–2c are the standard deviations of the perturbed VER profiles (dashed lines) with respect to the unperturbed profiles. It clearly shows that the peak variability is below the peak VER as described by *Liu and Swenson* [2003] for OH and O_2. This asymmetry in wave response arises primarily because of the large vertical gradient in [O] on the bottom side of the layer (Figure 1). For all three layers, the centroid heights of the standard deviation profiles are lower in altitude than that of the VER profiles by approximately 3 km. The thicknesses of the standard deviation profiles are ~2 km less than the thickness of the VER profiles. The quantitative comparisons are summarized in Table 1. The individual terms associated with the VER perturbation versus altitude for OH are illustrated by *Swenson and Gardner* [1998, Figure 7]. The quenching and wave induced temperature effects are higher in altitude and oppose the effects of the dominant term, which is the local change in O density. The VER expressions (2) and (3) are similar in forms and will have similar perturbation term profiles to that of OH.

[25] The temporal evolution of the disturbance in each layer is shown in Figures 2d–2f. The wave influences the volume emission rate to vary during the one period interval shown. However, the peak of the perturbation occurs at different times (phase) for the respective layers.

[26] The difference between the standard deviation and the VER profiles indicates that for zenith observations, the wave intensity information obtained is weighted by the standard deviation profile, rather than the VER profile. As a result, in the following simulations, the AGW amplitude deduced from I'/I for a given layer is defined as the amplitude at the peak of the standard deviation profile.

4.2. Variable λ_z and Constant β

[27] Here we present the results of gravity waves considering the variation of the vertical wavelength with a fixed damping rate. The CFs for temperature (CF_{Tm}) and intensity (CF_I) contrast each other, as illustrated Figure 3. While the CF_I increases asymptotically to ~ 5 for large vertical wavelength, the asymptotic value of CF_{Tm} is 1. However, for small vertical wavelengths, the values of CF_{Tm} decrease faster then CF_I because of the fact that the thickness of the VER is larger than that of the variance. The asymptotic value of CF_I for the OH layer is smaller; that is, the OH emission is less sensitive. Note in equations (2) and (3) that $\varepsilon_{O(^1S)}$ and ε_{O_2} are dependent on the 3rd power of the O density, while ε_{OH} depends on the 2nd power under normal conditions. The O_2(b) and $O(^1S)$ responses are quite similar because of their similar sensitivity to density perturbation and the similarity between their layer characteristics. Their centroid altitude are located around 95 and 97.3 km, respectively, ~2.3 km apart; and their layer thickness are ~9 km.

[28] We performed a least squares fit (not shown) on the modeled values of CF_I. The fitting expression describes an exponential increase until reaching the asymptotic coefficient c_0 in large vertical wavelength range. The analytical

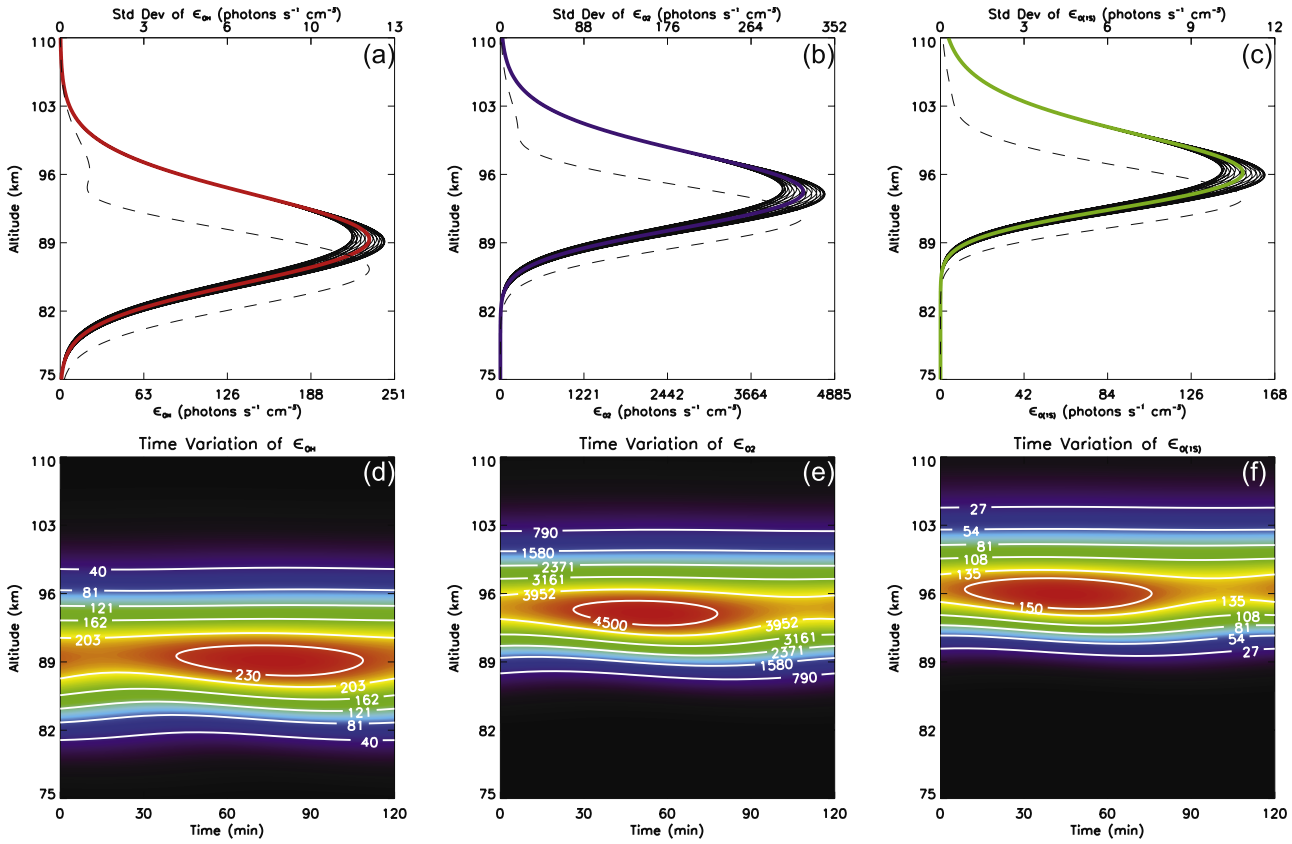

Figure 2. Airglow layers disturbed by a saturated gravity wave (β = 1) with period of 2 hours. Unperturbed volume emission rate profiles (thick color lines) for (a) OH, (b) O_2(b), and (c) O(^{1}S). The superimposed thin lines are the perturbed emission profiles computed each 15° for one wave period, while the dashed lines are the standard deviation profile calculated from the disturbed profiles. (d–f) Time variation of the volume emission rate for the same wave.

function adopted is:

$$\mathrm{CF} = c_0 - c_1 e^{-c_2(\lambda_z - 6\,\mathrm{km})^2} \tag{12}$$

The fitting coefficients and errors are in Table 2. The squared correlation coefficients of the fitting function are above 0.98 for all the layers. The fitting function well represents the CF_I values in the range of $\lambda > 6$ km. In practice, we don't recommend using the CF values for $\lambda <$ 10 km, and for this reason, the plots all have 10 km as the lower limit.

[29] Amplitude ratios for intensity are shown in Figure 4a. This parameter can be considered as an indicator of the degree of wave damping between layers. The ratios $I'_{O(1S)}/I'_{OH}$ and I'_{O2}/I'_{OH} are near constant for $\lambda >$ 20 km. Despite the invariance in the wave amplitude when

Table 1. Calculated Values of Centroid and Thickness (FWHM) for Undisturbed and Standard Deviation Profiles

	Unperturbed Profile		Standard Deviation Profile		Variation	
	Centroid Height	FWHM	Centroid Height	FWHM	$\Delta z_{Centroid}$	ΔFWHM
O(^{1}S)	97.3 (km)	9.3 (km)	94.3 (km)	7.2 (km)	3.0 (km)	2.1 (km)
O_2(b)	95.0 (km)	9.4 (km)	92.1 (km)	7.4 (km)	2.9 (km)	2.0 (km)
OH	89.9 (km)	10.9 (km)	86.8 (km)	8.7 (km)	3.1 (km)	2.2 (km)

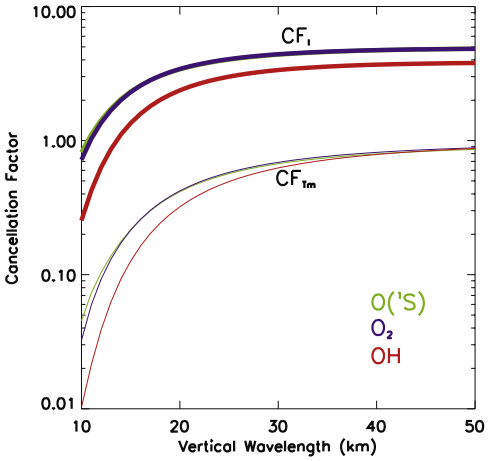

Figure 3. Cancellation factor of intensity (thick lines) and for weighted temperature (thin lines) of mesospheric airglow layers. Red, dark blue, and green colors represent the OH, O_2(b) and O(^{1}S) emissions, respectively. We assumed a wave period of 2 hours and β = 1 in this calculation.

Table 2. Coefficients and Associated Errors of the Fitting Function (Equation (11)) for the CF_I in the Airglow Layers

	c_0	c_1	c_2
$O(^1S)$	4.68 ± 0.03	3.73 ± 0.08	0.0060 ± 0.0003
$O_2(b)$	4.69 ± 0.03	3.86 ± 0.08	0.0064 ± 0.0003
OH	3.68 ± 0.02	3.41 ± 0.05	0.0053 ± 0.0002

$\beta = 1$, these amplitude ratios are not close to one because of the difference in the gain factor in different emissions. Figure 4b shows that the phase difference is sensitive to the vertical wavelength for a wave extending through the layers. The largest phase difference is between $O(^1S)$ and OH layers, changes from 60 to more than 150° in the range of $20 < \lambda < 50$ km. Since the phase difference is positive, the higher layers always lead the disturbance, in agreement with physical knowledge about the layer location in the atmosphere, i.e., downward phase propagation of an upward propagating gravity wave.

4.3. Variable λ_z and β

[30] Consideration is given to the effect of wave damping by varying the damping parameter β. β values other than 1 implies wave amplitude varying with altitude. We simulate wave propagation with different damping to examine the effects on the cancellation factor, the intensity to weighted temperature ratio, and the phase difference. *Liu and Swenson* [2003] showed that the damping rate may also change the centroid altitudes of the OH and $O_2(b)$ layers, and these changes in the altitude affect the phase difference.

[31] Consider first the cancellation factor for intensity, CF_I. Figure 5 shows the contours of the cancellation factor for three emissions, as a function of λ and β. The patterns are similar for all three airglow layers since all three layers have a similar thickness. Also, we note that a minimum value near $\beta = 1.2$ to 1.3 in the large vertical wavelength range. The cancellation factor is smaller in the OH than in the other two layers.

[32] The amplitude ratio and phase differences of the intensity present a very interesting behavior when both λ and β are changing. As expected, the amplitudes become small for large damping rate values as illustrated by the results showed in Figures 6a–6c. Because the wave amplitude is affected by the damping, the resulting perturbation on the emission profile becomes very small.

[33] The amplitude ratio is larger for $I_{O(1S)}/I_{OH}$ than for $I_{O(1S)}/I_{O2}$ (Figures 6b and 6c, respectively), and the phase difference is larger for the $O(^1S)$–OH layers and smaller for the $O(^1S)$–$O_2(b)$, because of the larger separation between $O(^1S)$ and OH than $O(^1S)$ and $O_2(b)$. The phase difference is positive indicating that the upper layers are leading the disturbance induced by an upward propagating gravity wave (downward phase progression).

[34] The amplitude ratio shown in Figures 6a–6c is not sensitive to the vertical wavelength variation for $\lambda > 20$ km. This suggests that solely from measurement of amplitude ratios among airglow layers, one can get a good estimate of the wave damping rate, regardless of the wave's vertical wavelength. Figures 6d–6f show the phase differences. Opposite to the amplitude ratios, the phase differences are sensitive to vertical wavelength while insensitive to the damping rate. Consequently, from the measured phase difference alone, one can get a good estimate of the vertical wavelength.

4.4. Momentum and Energy Fluxes

[35] The momentum and energy fluxes can be determined from the airglow images as well as their potential influence on the atmosphere by the momentum and energy flux convergence. Here we calculate the momentum and energy fluxes for an idealized wave in the same way that we treat a quasi-monochromatic wave observed in an airglow layer. Once the fluxes of momentum and energy are known in more than one layer, the effect of the dissipating waves on the atmosphere can be estimated from these models.

[36] An estimate of the vertical flux of horizontal momentum per unit volume is given by [see *Swenson et al.*, 2000]:

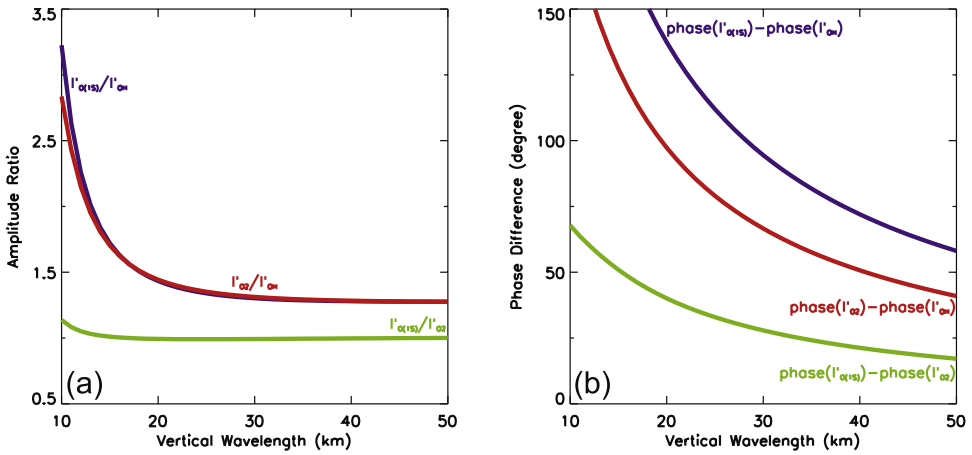

Figure 4. (a) Amplitude ratio and (b) phase difference of intensity between different airglow layers. Red, dark blue, and green colors represent relations between $O_2(b)$–OH, $O(^1S)$–OH, and $O(^1S)$–$O_2(b)$, respectively. We assumed a wave period of 2 hours and $\beta = 1$ (saturated wave) in this calculation.

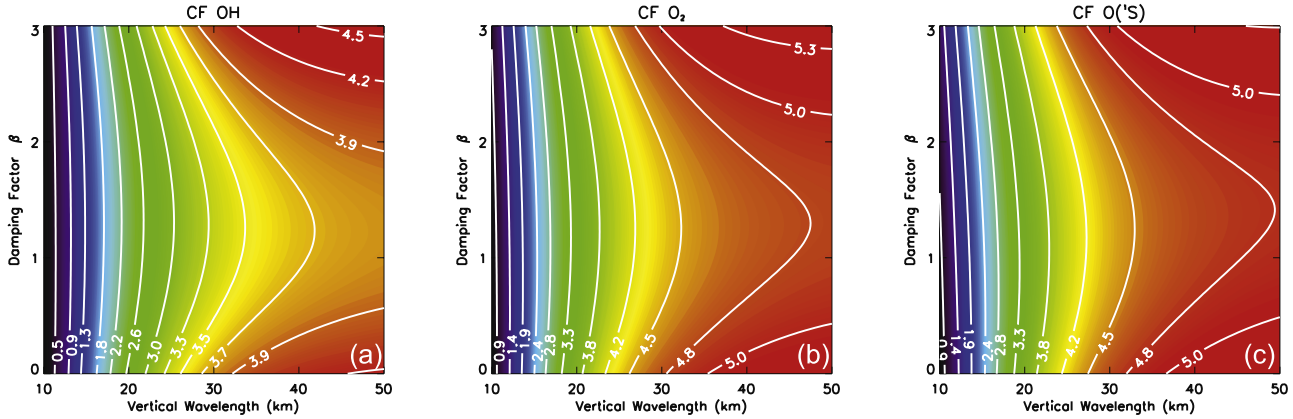

Figure 5. Cancellation factor of intensity with variable damping rates and vertical wavelengths, for (a) OH, (b) O_2(b), and (c) O(^{1}S) emissions.

$$F_M = \rho_u \langle u'w' \rangle = -\frac{\rho_u}{2}\frac{km}{m^2+\alpha^2}|\hat{u}|^2 = -\frac{\rho_u}{2}\frac{\omega^2 g^2 m}{N^4 k T_0^2}\left|\hat{T}\right|^2, \quad (13)$$

where $\alpha = 1/2H$, $|\hat{u}|$ and $|\hat{T}|$ the horizontal wind and temperature amplitudes, respectively, and the bracket indicates an average over one wave period. For a wave with eastward ($k > 0$) and downward ($m < 0$) phase progression the momentum flux is positive. The vertical flux of energy per unit volume is:

$$F_E = \frac{\rho_u}{2}\frac{m\omega}{m^2+\alpha}|\hat{u}|^2 = -\frac{\rho_u}{2}\frac{\omega^3 g^2 m}{N^4 k^2 T_0^2}\left|\hat{T}\right|^2 = \frac{\omega}{k}F_M. \quad (14)$$

Again the negative vertical wave number gives upward energy flux. The atmospheric density ρ_u decreases expo-

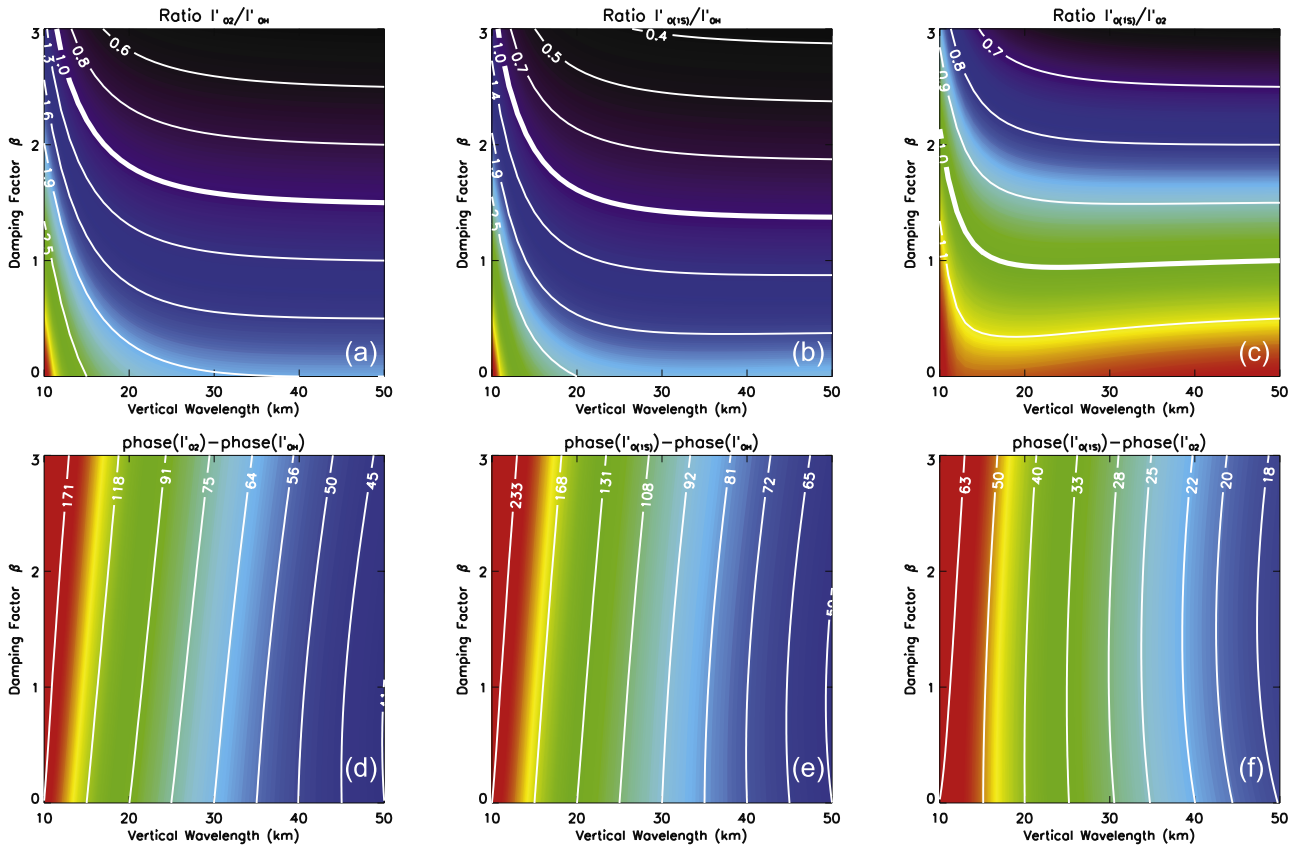

Figure 6. Amplitude ratio between (a) O_2(b)–OH, (b) O(^{1}S)–OH, and (c) O(^{1}S)–O_2(b) emissions as a function of the damping rate and vertical wavelength. Phase difference in degrees for (d) O_2(b)–OH, (e) O(^{1}S)–OH, and (f) O(^{1}S)–O_2(b) emissions as a function of the damping rate and vertical wavelength.

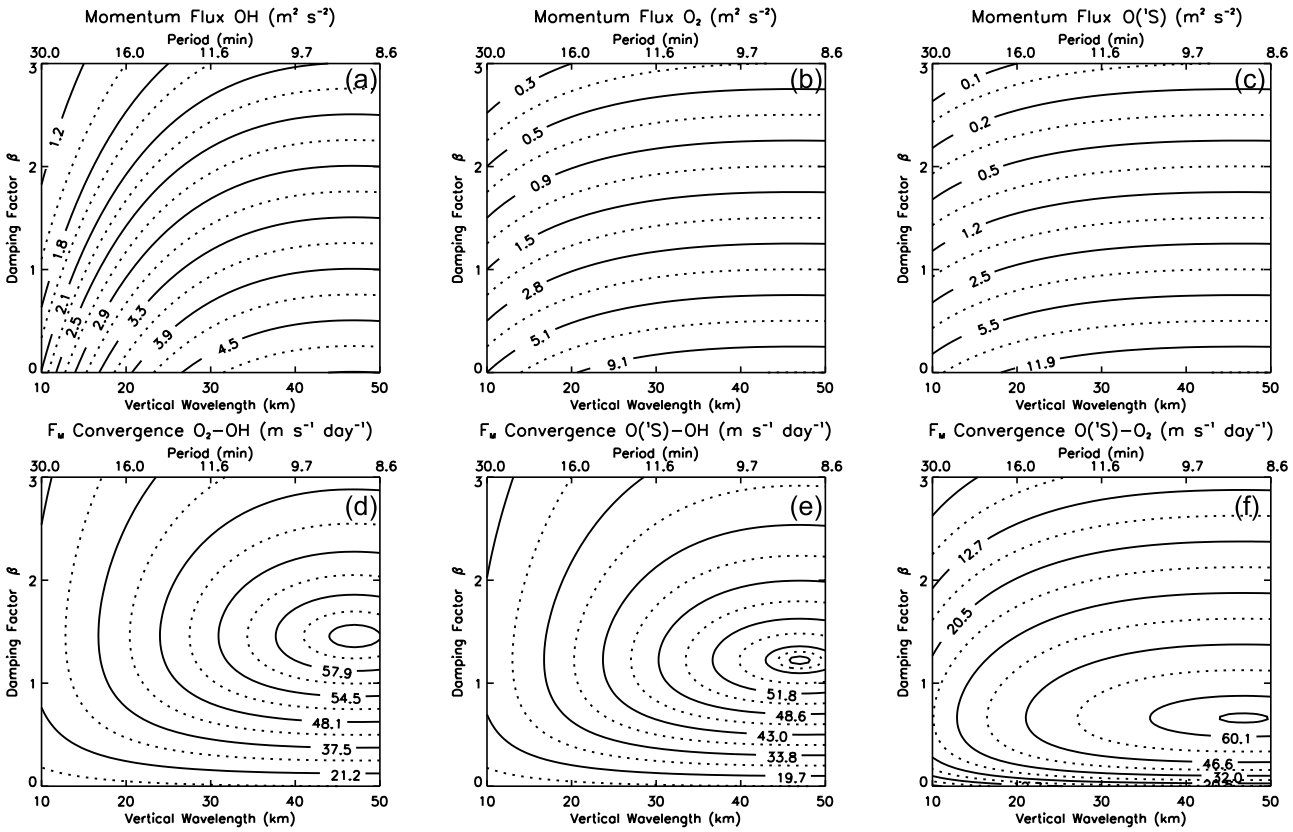

Figure 7. (a–c) Momentum flux and (d–f) momentum flux convergence. The relative temperature amplitude is 1% at 85 km. The horizontal wavelength is 60 km.

nentially as: $\sim\exp(-z/H)$, where for a freely propagating wave its amplitude increases as $\sim\exp(z/2H)$, therefore F_M and F_E are constant with altitude and the deposition of momentum and energy due to nondissipative AGWs is null. However, AGWs experiencing dissipation ($\beta > 0$) are expected to transfer momentum and energy to the background atmosphere, through the flux divergence which is proportional to the vertical derivative of the flux.

[37] To apply (13) and (14) to airglow data, the temperature amplitude needs to be deduced from measured airglow intensity amplitude through the CF_I, as *Swenson and Liu* [1998] did for the OH layer. The fluxes per unit mass are

$$F_M/\rho_u = -\frac{1}{2}\frac{\omega^2 g^2 m}{N^4 k}\left(\frac{I'/I_0}{\mathrm{CF_I}}\right)^2$$
$$F_E/\rho_u = -\frac{1}{2}\frac{\omega^3 g^2 m}{N^4 k^2}\left(\frac{I'/I_0}{\mathrm{CF_I}}\right)^2 \quad (15)$$

where I'/I_0 is the relative amplitude perturbation of the airglow intensity. The density and temperature used in these formulas were layer averages weighted by the standard deviation profile of each layer; the Brünt-Väisälä frequency N and the gravity acceleration g were calculated in each layer at the centroid altitude of the standard deviation profiles. The wave we consider has the same 1% amplitude in temperature at the reference altitude z_r = 85 km. We calculate the momentum and energy fluxes for each layer and then the flux convergences between layers.

[38] Figure 7 shows the momentum flux per unit mass F_M/ρ_u and flux convergence $-\rho_u^{-1}\partial F_M/\partial z$ as functions of the vertical wavelength and the damping rate for a fixed horizontal wavelength of 60 km. The wave period, ranging from 9 to 30 min, includes the high-frequency waves frequently observed in airglow image data. As expected, the momentum flux decreases with increasing damping rate; Comparing all 3 layers, we can see that the momentum flux is larger (smaller) in upper layers for smaller (larger) β. Note that the values of momentum flux are virtually the same when $\beta = 1$ because the wave amplitude is the same in all the layers in this special case. Figures 7d–7e show the flux convergence between layers. It has a peak near $\beta = 1$. Since F_M depends implicitly on β, it can be shown that ${}^1\partial F_M/\partial z$ is proportional to $\sim\beta\varepsilon^{(1-b)(z-zr)/H}$, which is a function increasing linearly with and decreasing exponentially with β. The maximum convergence is reached when $\beta_{\max} = \mathrm{H}/(z_1 - z_r)$, where z_l is the altitude between the layers where the flux convergence is calculated. For example, consider the flux convergence between O_2(b) and OH layers, where $z_l \sim 90$ km. With H$\sim$6 km at this level, $\beta_{\max} \sim 1.2$, which is where the maximum flux convergence is in Figure 7d. The positive flux convergence indicates that momentum is being deposited in the atmosphere. For small damping, the flux convergence is small and approaches zero when damping approaches zero.

[39] The same characteristics discussed above are also present in the energy flux F_E in Figure 8, except that the energy flux increases with λ^2. Larger energy flux conver-

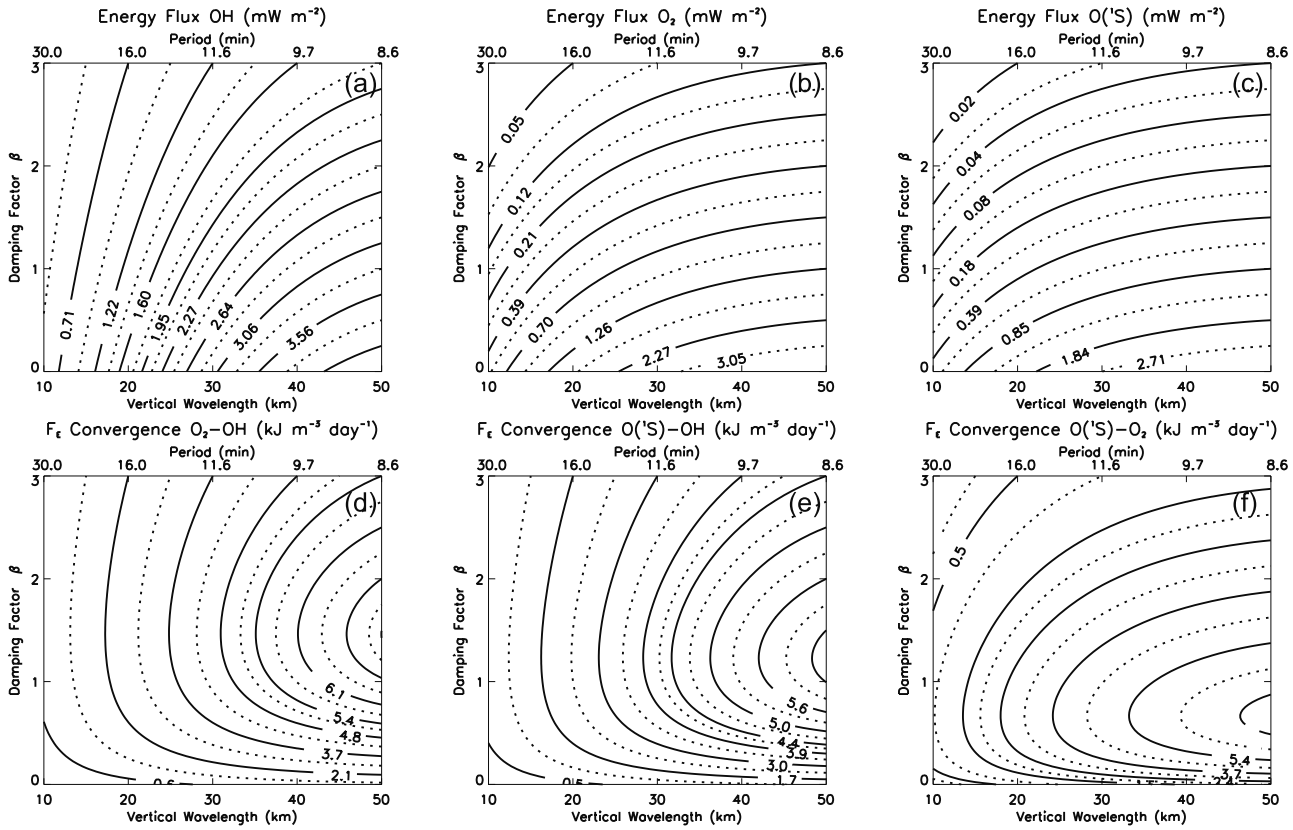

Figure 8. Same as Figure 7 but for (a–c) energy flux and (d–f) energy flux convergence.

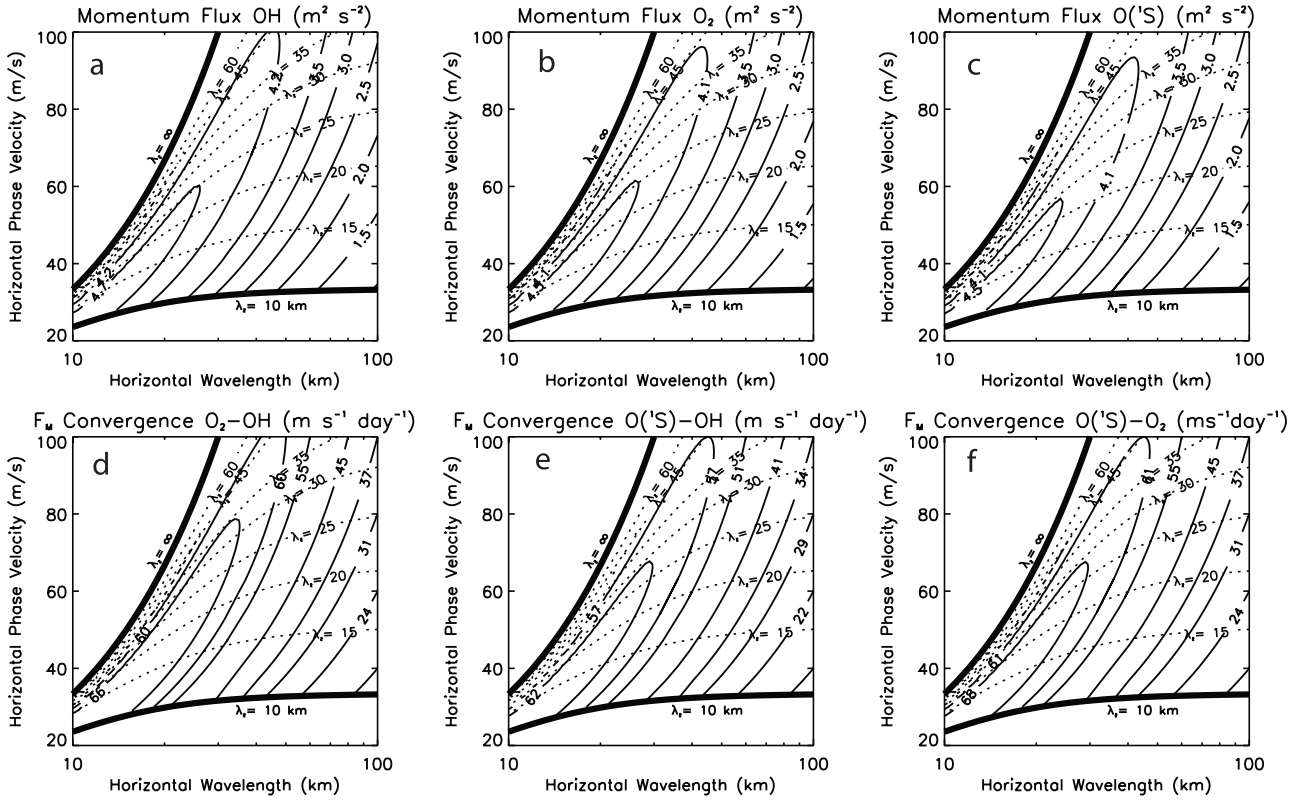

Figure 9. (a–c) Momentum flux and (d–f) momentum flux convergence for a saturated wave ($\beta = 1$). The relative temperature amplitude is 1%. Lines of constant vertical wavelength are showed as dotted lines.

gence is associated with larger λ and the peak value is also at $\beta = H/(z_l - z_r)$.

[40] In Figure 9 we present F_M/ρ_u and $-\rho_u^{-1}\partial F_M/\partial z$ as functions of horizontal wavelength and horizontal phase velocity for a fix damping rate $\beta = 1$. These will be easily applied in observations since horizontal wavelength and phase velocity are directly observed in airglow imagers. The saturated waves are also most typical in the mesopause region. Note that even though the values of F_M/ρ_u are quite similar in different layers because of similar wave amplitudes, $-\rho_u^{-1}\partial F_M/\partial z$ is still significant because of the density difference between the layers. Both the flux and flux convergence are larger for larger phase velocity (shorter periods) waves. This agrees with observational data that shows small temporal-scale waves carrying more momentum flux [e.g., *Vincent*, 1984]. The lines of constant vertical wavelengths are also drawn as dotted lines in the Figure 9. The top dotted lines for $\lambda \rightarrow \infty$ correspond to an upper limit of vertically propagating AGWs, beyond which the waves are evanescent. The lower limit ($\lambda < 10$ km) corresponds to waves that cannot be observed in zenith-viewed observations because of the finite thickness of the layers, i.e., the strong cancellation effect for short vertical-scale waves.

5. Summary

[41] The O(^{1}S) (green line) night airglow emission in response to atmospheric gravity wave (AGW) perturbations was modeled with a linear, one-dimensional model. The results were combined with previously modeled O_2(b, 0–1) Atmospheric band and OH Meinel band emission response [*Liu and Swenson*, 2003] to derive amplitude and phase relations among multiple airglow layers in response to gravity waves with various intrinsic parameters and damping rates (β). This one-dimensional model has a number of assumptions which include the following:

[42] 1. The wave amplitudes are small so that we can use the linear equations to describe AGWs using their polarization and dispersion relationships.

[43] 2. The background atmosphere specified by the MSIS00 model is unchanged by the waves. It determines the composition and temperature through which the waves are propagating.

[44] 3. The atmosphere is windless (and of course no shear with altitude). In practice, intrinsic wave periods need to be deduced to apply the results of the model. The background wind used to deduced the intrinsic period should be weighted by standard derivation profiles discussed in section 4.

[45] 4. The waves are propagating vertically (and are not ducted, for example). The waves are assumed to extend through the layers modeled.

[46] The simulations show that the vertical profile of the standard deviation of the perturbed green line volume emission rate (VER) has a centroid altitude that is 3 km lower and a full-width-half-maximum 2.1 km smaller than the unperturbed VER profile, similar to findings for the OH and O_2(b) band layers. Essentially, when one combines both the wave induced layer response in temperature, and the bottom layer response in VER, there become two distinct altitudes from each of the emissions to provide wave information, and with 3 layers, there are potentially 6 altitudes from which wave information originate. Wave phase and amplitudes for vertically propagating waves can be deduced from zenith observations of the layers. Airglow weighted responses to waves are related through a cancellation factor (CF) for both layer intensity and temperature (Figure 5). The vertical wavelength can be deduced from the relative phase information from three airglow layers separated in altitudes (Figure 6).

[47] The vertical flux of horizontal momentum associated with gravity waves is deduced from the intrinsic wave parameters. Figure 7 describes the vertical flux of horizontal momentum for high-frequency waves, which are shown for all three layers for various degrees of damping. Figure 8 denotes the energy flux associated with a 1% amplitude at 85 km, for various damping rates, from $\beta = 0$ (freely propagating), to $\beta = 1$ (saturated), and $\beta > 1$ (heavily damped). One should note in Figure 8, for example, that a 1% amplitude, high-frequency wave with $\lambda \sim 30$ km, contains an upward flux of energy of a few mW m^{-2}. Given a global flux of waves reaching these altitudes from below, this is a dominant energy flux into the MLT region.

[48] Wave damping versus altitude is used to deduce the flux divergence and local accelerations resulting from damped waves. Figure 9 summarizes the vertical flux of momentum for an assumed 1% (saturated) wave, as well as the flux divergence and accelerations associated with this damping assumption. The calculations are useful in calculating wave information and wave effects on the atmosphere from multiwavelength, zenith airglow observations. Figure 9 is intended to be a useful tool for directly interpreting fluxes of airglow measurements where the saturated conditions are measured. Figure 6 are plots which, with measurements of phase between layers for wave induced intensity perturbations, provide reference to deduce the vertical wavelength and damping factor. We caution the interpretation when using Figure 6 (or Figure 9) of phase differences assume constant wind versus altitude.

[49] Statistical measurements of global fluxes of AGW energy and momentum are important measurements, and the tools provided a simplified method to standardize for comparison. It is proposed that this model be a standard reference where comparisons can be made from measurements at different locations and times, and will provide a top level estimate of the values under the simplified conditions incorporated in this model.

[50] **Acknowledgments.** This work has been supported partially by the NSF Atmospheric Sciences grant NSF ATM 0338425 and NASA grants NAG 5-12952 and NAG 5-13593. This work was also supported by the Brazilian funding agency CNPq (National Counsel of Technological and Scientific Development), under grant 200195/2005-0, and we would like to thank them for their scientific engagement.

References

Barth, C. A. (1961), 5577-angstrom airglow, *Science*, *134*, 1426–1430.

Coble, M. R., G. C. Papen, and C. S. Gardner (1998), Computing two-dimensional unambiguous horizontal wavenumber spectra from OH airglow images, *IEEE Trans. Geosci. Remote Sens.*, *36*, 368–382.

Espy, P. J., G. O. L. Jones, G. R. Swenson, J. Tang, and M. J. Taylor (2004), Seasonal variations of the gravity wave momentum flux in the Antarctic mesosphere and lower thermosphere, *J. Geophys. Res.*, *109*, D23109, doi:10.1029/2003JD004446.

Fritts, D. C., and T. J. Dunkerton (1985), Fluxes of heat and constituents due to convectively unstable gravity waves, *J. Atmos. Sci.*, *42*, 549–556.

Fritts, D., and R. Vincent (1987), Mesospheric momentum flux studies at Adelaide, Australia: Observations and a gravity wave-tidal interaction model, *J. Atmos. Sci.*, *44*, 605–619.

Gavrilyeva, G. A., and P. P. Ammosov (2002), Wave structures imaged in near-infrared nightglow at Yakutsk, *J. Atmos. Terr. Phys.*, *64*, 1117–1120.

Hecht, J. H., R. L. Walterscheid, and M. N. Ross (1994), First measurements of the two-dimensional horizontal wave number spectrum from CCD images of the nightglow, *J. Geophys. Res.*, *99*, 11,449–11,460.

Hecht, J. H., R. L. Walterscheid, and R. A. Vincent (2001), Airglow observations of dynamical (wind shear-induced) instabilities over Adelaide, Australia, associated with atmospheric gravity waves, *J. Geophys. Res.*, *106*, 28,189–28,198.

Hines, C. O. (1960), Internal atmospheric gravity waves at ionospheric heights, *Can. J. Phys.*, *38*, 1441–1481.

Krassovsky, V. I. (1972), Infrasonic variations of the OH emission in the upper atmosphere, *Ann. Geophys.*, *28*, 739–746.

Liu, A. Z., and G. R. Swenson (2003), A modeling study of O-2 and OH airglow perturbations induced by atmospheric gravity waves, *J. Geophys. Res.*, *108*(D4), 4151, doi:10.1029/2002JD002474.

Makhlouf, U. B., R. H. Picard, and J. R. Winick (1995), Photochemical-dynamical modeling of measured response of airglow to gravity waves: 1. Basic model for OH airglow, *J. Geophys. Res.*, *100*, 11,289–11,311.

McDade, I. C., D. P. Murtagh, R. G. H. Greer, P. H. G. Dickinson, G. Witt, J. Stegman, E. J. Llewellyn, L. Thomas, and D. B. Jenkins (1986), ETON 2: Quenching parameters for the proposed precursors of O2 ($^{b1}\Sigma$) and O (^{1}S) in the terrestrial nightglow, *Planet. Space Sci.*, *34*, 789–800.

McDade, I. C., E. J. Llewellyn, D. P. Murtagh, and R. G. H. Greer (1987), ETON 5: Simultaneous rocket measurements of the OH Meinel $\Delta\nu = 2$ sequence and (8–3) band emission profiles in the nightglow, *Planet. Space Sci.*, *35*, 1137–1147.

Murtagh, D. P., G. Witt, J. Stegman, I. C. McCade, E. J. Llewellyn, F. Harris, and R. G. H. Greer (1990), An assessment of proposed O (^{1}S) and O2 ($^{b1}\Sigma_{+}$) nightglow excitation parameters, *Planet. Space Sci.*, *38*, 43–53.

Nakamura, T., A. Higashikawa, T. Tsuda, and Y. Matsushita (1999), Seasonal variations of gravity wave structures in OH airglow with a CCD imager at Shigaraki, *Earth Planets Space*, *51*, 897–906.

Nakamura, T., T. Tsuda, R. Maekawa, M. Tsutsumi, K. Shiokawa, and T. Ogawa (2001), Seasonal variation of gravity waves with various temporal and horizontal scales in the MLT region observed with radar and airglow imaging, *Adv. Space Res.*, *27*(10), 1737–1742.

Picone, J. M., A. E. Hedin, D. P. Drob, and A. C. Aikin (2002), NRLMSISE-00 empirical model of the atmosphere: Statistical comparisons and scientific issues, *J. Geophys. Res.*, *107*(A12), 1468, doi:10.1029/2002JA009430.

Suzuki, S., K. Shiokawa, Y. Otsuka, T. Ogawa, and P. Wilkinson (2004), Statistical characteristics of gravity waves observed by an all-sky imager at Darwin, Australia, *J. Geophys. Res.*, *109*, D20S07, doi:10.1029/2003JD004336.

Swenson, G. R., and C. S. Gardner (1998), Analytical models for the responses of the mesospheric *OH** and Na layers to atmospheric gravity waves, *J. Geophys. Res.*, *103*, 6271–6294.

Swenson, G. R., and A. Z. Liu (1998), A model for calculating acoustic gravity wave energy and momentum flux in the mesosphere from OH airglow, *Geophys. Res. Lett.*, *25*, 477–480.

Swenson, G. R., R. Haque, W. Yang, and C. S. Gardner (1999), Momentum and energy fluxes of monochromatic gravity waves observed by an OH imager at Starfire Optical Range, New Mexico, *J. Geophys. Res.*, *104*, 6067–6080.

Swenson, G. R., M. J. Alexander, and R. Haque (2000), Dispersion imposed limits on atmospheric gravity waves in the mesosphere: Observations from OH airglow, *Geophys. Res. Lett.*, *27*, 875–878.

Swenson, G. R., A. Z. Liu, F. Li, and J. Tang (2003), High frequency atmospheric gravity wave damping in the mesosphere, *Adv. Space Res.*, *32*(5), 785–793.

Tang, J., G. R. Swenson, A. Z. Liu, and F. Kamalabadi (2005), Observational investigations of gravity wave momentum flux with spectroscopic imaging, *J. Geophys. Res.*, *110*, D09S09, doi:10.1029/2004JD004778.

Taylor, M. J., Y. Y. Gu, X. Tao, C. S. Gardner, and M. B. Bishop (1995), An investigation of intrinsic gravity-wave signatures using coordinated lidar and nightglow image measurements, *Geophys. Res. Lett.*, *22*, 2853–2856.

Vincent, R. A. (1984), Gravity-wave motions in the mesosphere, *J. Atmos. Terr. Phys.*, *46*, 119–128.

Walterscheid, R. L., G. Schubert, and J. M. Straus (1987), A dynamical-chemical model of wave-driven fluctuations in the OH nightglow, *J. Geophys. Res.*, *92*, 1241–1254.

Zhang, S. P., R. H. Wiens, and G. Shepherd (1993), Gravity waves from O2 nightglow during AIDA '89 campaign II: Numerical modeling of the emission rate/temperature ratio, *J. Atmos. Terr. Phys.*, *55*, 377–395.

Zhao, Y., M. J. Taylor, and X. Chu (2005), Comparison of simultaneous Na lidar and mesospheric nightglow temperature measurements and the effects of tides on the emission layer heights, *J. Geophys. Res.*, *110*, D09S07, doi:10.1029/2004JD005115.

D. Gobbi, Aeronomy Division, National Institute for Space Research, São José dos Campos, 12201-970 SP, Brazil.

A. Liu, G. Swenson, and F. Vargas, Department of Electrical and Computer Engineering, University of Illinois at Urbana-Champaign, Urbana, IL 61801, USA. (fabioaugustovargas@gmail.com)